On the sub-/super-radiance of cold atom gases organized in periodic medium

Alexandre Menard (M1-Mag2 Fundamental Physics)
supervised by Etienne Brion
in the Theory team

12 May - 1 August 2025

Laboratoire Collisions, Agrégats et Réactivités - UMR 5589
118 Route de Narbonne - Bâtiment FeRMI (3R4)
31062 Toulouse Cedex 09

Abstract

This work investigates the collective scattering properties of cold atomic gases arranged in a one-dimensional optical lattice, with a focus on sub- and super-radiant phenomena. Using a quantum microscopic model, we study both the steady-state and dynamical scattering regimes, accounting for dipole-dipole interactions and spontaneous emission. Our analysis reproduces key experimental features such as Bragg reflection and the emergence of photonic band gap (**PBG**), while also revealing the dependence of reflectivity on atom number, density, lattice periodicity, and detuning. We demonstrate that optical depth plays a central role in shaping the reflection response and highlight the conditions under which off-resonant driving optimizes reflectivity. Furthermore, we extend the study to the dynamical regime, providing insights into decay rates and their scaling with system size, in line with recent experimental observations of superradiant emission.

CONTENTS

INTRODUCTION

The study of collective interaction of light and matter at the quantum level has developed from the pioneering theoretical work of Dicke in the 1950s [6], who introduced the notion of superradiance. This phenomenon describes enhanced collective emission caused by constructive interference between atoms. Building on this work, the concept of subradiance emerged, wherein the spontaneous emission of atoms can be suppressed.

Over the past decades, these ideas have been incorporated into protocols for quantum information storage and processing, notably through the use of atomic ensembles and highly ordered atomic arrays. The development of photonic nanostructures (such as nanofibers [7] or integrated cavities) has enabled controlled guidance of light along desired channels, paving the way for what is now referred to as "selective radiance" [7,8]. These concepts suggest that major improvements are possible in the fidelity of photonic storage, a key challenge in building quantum simulators and quantum memory.

A major challenge in the development of quantum memory lies in both the information lifetime and fidelity. It was shown that arrays of N atoms can be used as a photonic memory, with a fidelity that increases exponentially with the number of atoms [7]. This fidelity arises from the combination of subradiance into unwanted modes, and superradiance into modes used for information storage.

One the one hand, sub/super-radiance in spherical clouds has been studied under continuous approximation in [9] and experimentally in [10]. On the other hand, atoms in one dimensionnal optical lattice of cold atom gases in the form of periodic disks has been the center of many interests notably in [11–14].

In this study, we investigate the scattering of a continuous laser beam by such a periodic atomic structure using a quantum microscopic model. This phenomenon has already been widely studied in the literature, both experimentally and theoretically. We also examine the lesser-known dynamic response of the system to the sudden extinction of the incoming field.

I. EXPERIMENTAL SETUP

The layout of the experiment is shown in Fig. 1 and is motivated by an existing setup at the INPHYNI [15] and a previous experiment in Tübingen [13]. It consists of the periodic arrangement along the propagation axis z of N_d disks of thickness a and radius R_d evenly spaced with an interlayer d. N_a atoms are randomly distributed within each disk. Although a Gaussian distribution in each direction would better fit the true experimental setup, we will assume a uniform distribution but with reduced transversal dimension. Experimentally, the lattice is created using a vapor of ^{87}Rb confined in a Magneto-Optical Trap (MOT) and released into a dipole trap formed by a laser of wavelength λ_{dip}. By employing a highly reflective mirror, a standing wave with a periodicity of $\lambda_{\text{dip}}/2$ is generated, in which the atoms settle at the potential wells (see [13] for further details on the lattice formation process).

An incident probe beam of wavevector $k = 2\pi/\lambda$ impinges the system at an angle θ_i relative to the lattice axis (z-axis). As the beam encounters each disk, atoms are driven to their excitation state with a probability β_i, and reemit light in all directions. In this situation, a transmitted beam is observed in the same direction as the incident one, while a beam is reflected with an angle $\theta_r \approx \theta_i$ relative to the z-axis.
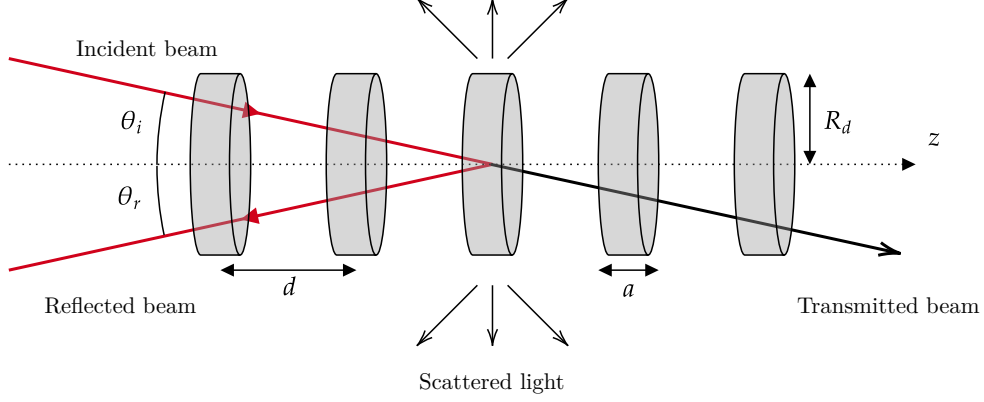
Fig. 1: Representation of the physical system

This type of setup has been studied in the transfer matrix framework, which however fails to describe the diffusion of light via spontaneous emission. This leads us to introduce a quantum microscopic model for the collective scattering between atoms accounting for spontaneous emission and diffusion.

II. Collective scattering with a microscopic model

We consider an ensemble of N scatterers with two levels $|g\rangle$ and $|e\rangle$ and an atomic transition frequency ω_a. We adopt a semi-classical model in which each scatterer has a classical position $\boldsymbol{r_i}$ and the classical incident electric field $\boldsymbol{E}_L$, either a plane-wave or a Gaussian beam. For the whole derivation, we take a plane-wave for simplicity with $\boldsymbol{E}_L(\boldsymbol{r}_i) = E_0\boldsymbol{u}\cos(\omega_L t - \boldsymbol{k}_L \cdot \boldsymbol{r}_i)$, where E_0 may be time dependant. The nature of the wave is of no importance since only the time dependance is involved. For the full derivation, readers may refer to [16]. The total Hamiltonian $\hat{H}$ is split into three components:

$$
\begin{aligned}
\hat{H}_0 &= -\sum_{j=1}^{N} \frac{\hbar\omega_a}{2}\sigma_{zj} + \sum_{\boldsymbol{k}} \hbar\omega_k a_k^\dagger a \\
\hat{H}_L &= -\sum_{j=1}^{N} \boldsymbol{d_j} \cdot \boldsymbol{E}_L(\boldsymbol{r_j}, t) \\
\hat{H}_Q &= \hbar \sum_{j=1}^{N}\sum_{\boldsymbol{k}} \sqrt{\frac{\omega_k}{2\hbar\varepsilon_0 V_{\text{ph}}}}\left[\hat{a}_k^\dagger \sigma_j e^{-i\boldsymbol{k}\cdot\boldsymbol{r}_j} + h.c\right] \\
\hat{H} &= \hat{H}_0 + \hat{H}_L + \hat{H}_Q
\end{aligned}
\tag{1}
$$

where $\hat{a}_k$ is the annihilation operator of the mode $\boldsymbol{k}$, $\sigma_i = |g_i\rangle\langle e_i|$, σ_{zj} the z Pauli matrix and $\hat{\boldsymbol{d}}_i = \left(\boldsymbol{d_{eg}}|e_i\rangle\langle g_i| + \boldsymbol{d_{eg}}^*|g_i\rangle\langle e_i|\right)$ the dipole operator for the i-th atom.

For a brief description, $\hat{H}_0$ corresponds to sum of the energies of the isolated two-level scatterers, $\hat{H}_L$ is the dipolar interaction between atomic dipoles and the classical field, and $\hat{H}_Q$ is the quantum light-matter interaction between the two level scatterers and the quantized electromagnetic field.

We switch to the new picture defined by $|\Psi\rangle \mapsto |\tilde{\Psi}\rangle = U^\dagger(t)|\Psi\rangle$ with:

$$
\hat{U}(t) = \exp\left(\sum_j i\frac{\omega_L t}{2}\sigma_{zj} - it\sum_{\boldsymbol{k}} \hbar\omega_k a_k^\dagger a\right)
\tag{2}
$$

5

In this frame, the Hamiltonian takes the form:

$$\hat{H}_I = \hat{H}_{0,I} + \hat{H}_{L,I} + \hat{H}_{Q,I} \tag{3}$$

with (A) the non interacting contribution:

$$\begin{aligned}
\hat{H}_{0,I} &= U^\dagger \hat{H}_0 U - i\hbar U^\dagger \frac{\mathrm{d}U}{\mathrm{d}t} \\
&= \sum_{j=1}^{N} \frac{\hbar\Delta}{2} \sigma_{zj}
\end{aligned} \tag{4}$$

where we introduced $\Delta \equiv \omega_L - \omega_a$, the laser detuning from the atomic transition frequency, (B) the laser hamiltonian $\hat{H}_{L,I}$:

$$\begin{aligned}
\hat{H}_{L,I} &= \hat{U}(t)^\dagger \hat{H}_L \hat{U}(t) \\
&= \frac{1}{2} \sum_{j=1}^{N} \left[\Omega E_0 e^{i\boldsymbol{k}_L \cdot \boldsymbol{r_j}} + \Omega^* E_0 e^{i2\omega_L t - i\boldsymbol{k}_L \cdot \boldsymbol{r_j}} \right] \sigma_j^\dagger + h.c \\
&\overset{\mathrm{RWA}}{\approx} \hbar \sum_{j=1}^{N} \left(\frac{\Omega}{2} \sigma_j^\dagger E_0 e^{i\boldsymbol{k}_L \cdot \boldsymbol{r_j}} + h.c \right)
\end{aligned} \tag{5}$$

where we introduced the laser Rabi frequency $\Omega = -(\boldsymbol{d_{eg}} \cdot \boldsymbol{u})/\hbar$ and neglected exponentials involving $2\omega_L$ as oscillations will average to zero on any accessible time scale next to non rotating exponentials.

and (C), the quantum light-matter interaction hamiltonian as :

$$\hat{H}_{Q,I} \approx \sum_{j=1}^{N} \sum_{\boldsymbol{k}} \left[g_k \hat{a}_k^\dagger \sigma_j e^{i(\omega_k - \omega_L)t - i\boldsymbol{k} \cdot \boldsymbol{r_j}} + h.c \right] \tag{6}$$

where $g_k = -d_{eg} \sqrt{\frac{\omega_k}{2\hbar\varepsilon_0 V_{\mathrm{ph}}}}$

The Heisenberg equations in this picture take the forms:

$$\begin{aligned}
\frac{\mathrm{d}\sigma_j}{\mathrm{d}t} &= \frac{1}{i\hbar} \left[\sigma_j, \hat{H} \right] = i\Delta_0 \sigma_j - i\frac{\Omega}{2} \sigma_{zj} E_L(\boldsymbol{r_j}) - i\sum_{\boldsymbol{k}} g_k \sigma_{zj} \hat{a}_k e^{-i(\omega_k - \omega_0)t + i\boldsymbol{k} \cdot \boldsymbol{r_j}} \\
\frac{\mathrm{d}\hat{a}_k}{\mathrm{d}t} &= \frac{1}{i\hbar} \left[\hat{a}_k, \hat{H} \right] = -ig_k e^{i(\omega_k - \omega_0)t} \sum_{j=1}^{N} \sigma_j e^{-i\boldsymbol{k} \cdot \boldsymbol{r_j}}
\end{aligned} \tag{7}$$

In the linear (i.e. single excitation) regime and Markov approximation (a photon will not interact back with the atom), formally integrating $\hat{a}_k$ and substituting in (7) leads to:

$$\frac{\mathrm{d}\sigma_j(t)}{\mathrm{d}t} = i\Delta_0 \sigma_j(t) - i\Omega \hat{I}_j e^{i\boldsymbol{k}_L \cdot \boldsymbol{r_j}} - \frac{\Gamma}{2} \sum_{m=1}^{N} \frac{e^{ik_L \|\boldsymbol{r_m} - \boldsymbol{r_j}\|}}{ik_L \|\boldsymbol{r_m} - \boldsymbol{r_j}\|} \sigma_m(t) \tag{8}$$

with $\hat{I}_j$ the identity operator for the j-th atom.

Assuming the following Ansatz for the wavefunctions:

$$|\Psi(t)\rangle \approx \alpha(t)|g\rangle + \sum_{j=1}^{N} \beta_j(t)|e_j\rangle \tag{9}$$

which restricts the Hilbert space to the ground and single excited states, we have $\langle\sigma_j\rangle \approx \beta_j$, and Eq. (9) gives:

$$\frac{d\beta_i(t)}{dt} = \left(i\Delta_0 - \frac{\Gamma}{2}\right)\beta_i(t) - \frac{\Gamma}{2}\sum_{k\neq i}\frac{e^{ik_L\|r_i-r_k\|}}{ik_L\|r_i-r_k\|}\beta_k(t) - i\frac{\Omega}{2}E_L(r_i) \tag{10}$$

Solving this last equation yields the single-excitation probability of each scatterer, from which we deduce the total scattered field as the sum of the fields radiated in free-space by each dipole (j).

$$E_s(r,t) = -\frac{\hbar\Gamma}{d_{eg}}\sum_j\frac{e^{ik_L\|r-r_j\|}}{ik_L\|r-r_j\|}\beta_j(t) \tag{11}$$

III. STATIONNARY SCATTERING

When the system is driven by a continuous wave probe beam of constant amplitude E_0, it reaches a steady state. The stationnary amplitudes β_i are deduced from (10) in which we set $d\beta_i\,/\,dt = 0$ or in matrix form:

$$M \cdot \beta = \frac{i}{2}E \tag{12}$$

with matrix elements:

$$M_{ij} = \left(i\Delta - \frac{\Gamma}{2}\right)\delta_{ij} - \frac{\Gamma}{2}\frac{e^{ik_L\|r_i-r_j\|}}{ik_L\|r_i-r_j\|} \tag{13}$$
$$E_i = \Omega E_0 \cdot G(r_i)$$

where $G(r_i)$ is either a gaussian or plane wave function of the position r.

For the present work, we use a Gaussian beam such that:

$$G(r,z) = \frac{w(0)}{w(z)}e^{-\frac{r^2}{w^2(z)}}e^{-ik_Lz-ik_L\frac{r^2}{2R(z)}-i\varphi} \tag{14}$$

with $w(z)$ the "waist" at z, $R(z)$ the radius of curvature and φ is the Gouy phase.

Solving the stationnary equation (12) is straightforward and only involves matrix inversion, and more precisely least square linear system solving to retrieve the steady state β, although solving such a system may be lengthy.

A. Reflection of a resonant probe beam ($\Delta = 0$)

We plotted the scattered light in the xOz plane in Fig. 2 and also trough the sphere of radius $R = 10^4\lambda$ in Fig. 3 for $N_a = 5000$ atoms distributed over $N_d = 80$ disks of thickness $a = 0.07\lambda$ and radius $R_d = 9\lambda$. For now, we assume a lattice periodicity d fulfilling the Bragg condition:

$$d = \frac{\lambda}{2\cos(\theta_i)} \tag{15}$$

which ensures that the waves reflected upon two consecutive disks are in phase.
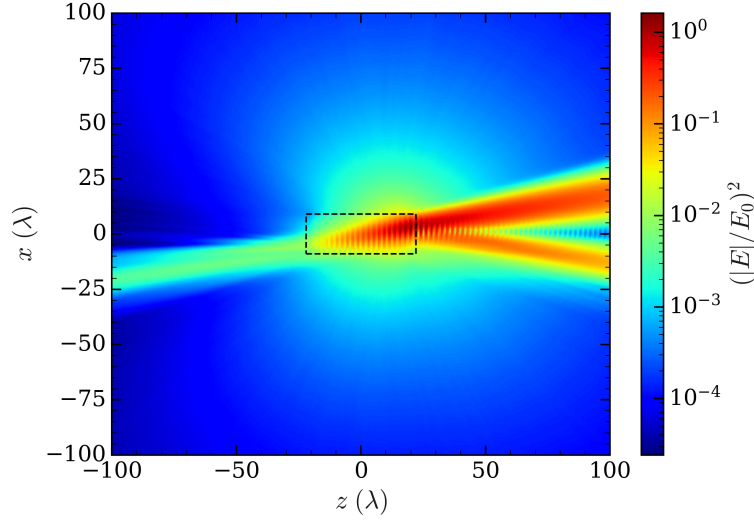
Fig. 2: Intensity of the scattered light in the (xOz) plane for $N_a = 5000$ atoms distributed uniformly over $N_d = 80$ disks of thickness $a = 0.07\lambda$, radius $R_d = 9\lambda$ and prepared in the Bragg condition of $\theta_{\text{bragg}} = 10°$. The probe beam is resonant with the atomic transition ($\Delta = 0$), with an incident angle of $\theta_i = 10°$ and a waist $w_0 = 4\lambda$. This image is the average intensity of 5000 random configurations. The dashed black box materializes the boundary of the lattice.
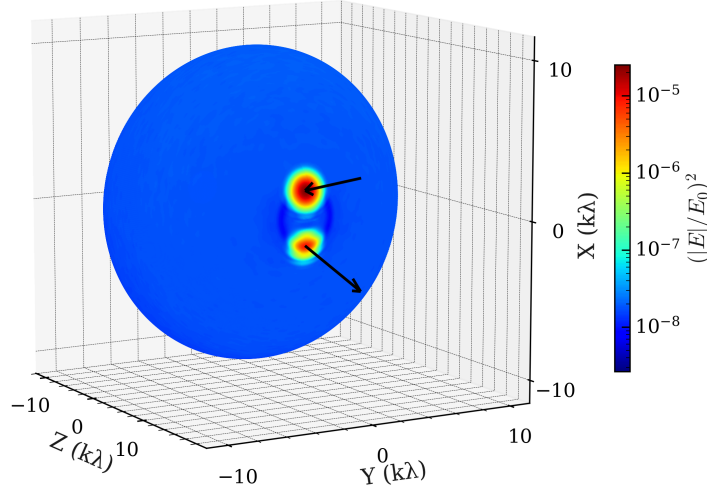
Fig. 3: Intensity of scattered light on the sphere at $R = 10^4\lambda$ for the same configuration as in Fig. 2. This image is the average of 5000 random configurations. Arrows show incident and reflected beam.

One should note that even for a lattice periodicity set in a Bragg scattering condition, looking at the scattered field (11), there are no evidences that the total field may shows any reflection in this very Bragg direction of $\theta = 10°$. However, in both cases in Fig. 2 and Fig. 3, scattered light exhibits a reflected beam in the Bragg direction (see Fig. 4) and a transmitted beam in the same incident direction.

8
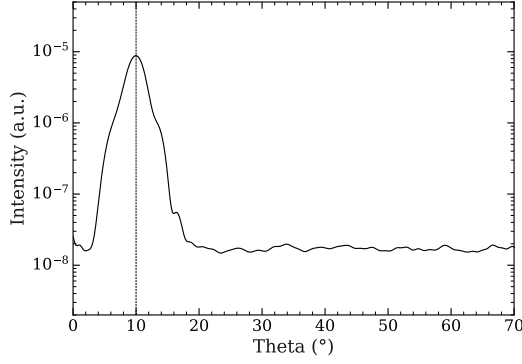
Fig. 4: Scattered intensity along θ direction (from z-axis towards reflected beam) for $\varphi = \pi$ for Fig. 3.

Energy conservation has been verified with a conservation up to $\approx 3\%$. The $\approx 3\%$ loss we observe most probably results from the erroneous counting of a part of the output energy in the input energy. This imprecision itself originates from the numerical method we use to estimate those energies: we arbitrarily choose portions of the sphere around the incident and reflected beam centers, on which we compute input and output intensities. In the input region, however, scattered light back in the incident direction is also present which leads to an overestimated value of the input energy and the small violation of energy conservation we noticed above.

Finally, an unexpected phenomenon is observed in the $\theta = 10°$ ring around the z-axis out of the xOz plane, i.e a minimum of intensity. This behavior indicates the emergence of a photonic band gap [13] for incident light along this specific direction. In this case, propagation is effectively 'forbidden' in the lattice resulting in strong reflection, while scattered light is also weakly emitted in the Bragg direction.

B. Bragg scattering condition

Strictly speaking, the Bragg condition we mentioned above applies to periodic continuous media. Bragg reflection is therefore expected to emerge from our microscopic model in the limit of large atom numbers and high atomic densities. For the sake of computation feasibility, we are however forced to consider systems with few thousands of atoms and few tens of disks, as in Fig. 2.

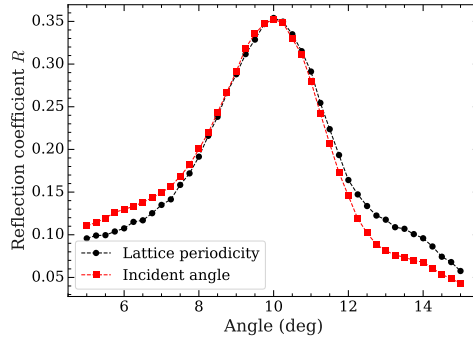Fig. 5: Reflection coefficient R as a function of (i) the incident beam angle with fixed lattice period d satisfying the Bragg condition $d = \lambda/2\cos(\theta)$ for the Bragg angle $\theta_i = 10°$ (red curve); (ii) the lattice period through the Bragg angle $\theta_i = \text{acos}(\lambda/2d)$ while fixing the incident beam angle at 10°. The lattice parameters are the same as in Fig. 2.

In Fig. 5 we analyze the reflection coefficient R either (A) varying the incident beam angle while keeping the lattice period constant at the value $d = \lambda/2\cos(\theta_i)$ for a Bragg angle $\theta_i = 10°$ (red curve) or (B) setting the incident beam angle at $10°$ while varying the lattice periodicity d or equivalently the Bragg angle $\theta_{\text{bragg}} = \text{acos}(\lambda/2d)$ (black curve). In both cases, the optimal reflection coefficient is achieved when the lattice periodicity satisfies Bragg's condition for an incident probe beam angle of $10°$. The overall angular dependence follows a similar trend close to the Bragg's angle, with only minor variations at larger angles which can be attributed to optical depth effects. Indeed, changing the incident angle is not strictly equivalent to modifying the lattice periodicity: decreasing the incident angle effectively increases the number of disks encountered by the beam, resulting in a greater optical depth. Nevertheless, within the considered angular range, optical depth effects remain small but are expected to become more significant at larger angles. Even if both dependances are similar, varying lattice periodicity is much closer to experimental setup where it is far easier to control the dipole trap creating potential well (and thus the lattice periodicity d) than changing the angle of incidence.

The observed width of the reflection coefficient curve essentially results from the convolution of the lattice's reflection response with the spatial profile of the beam, which has a waist of $w_0 = 4\lambda$ and divergence $\theta \approx 4.5°$. Consequently, even at other angles, a portion of the beam can still partially satisfy Bragg's condition, leading to a reduced but non-zero reflection coefficient.

In what follows unless otherwise stated, we assume the Bragg's condition (15) is fulfilled for an optimal reflection of the probe beam.

C. Reflectivity, atoms number, disks number, lattice periodicity and detuning

From Fig. 2, Fig. 3 and Fig. 4, we expect a reflected beam in the Bragg direction depending on the distance between each disk. We thus have two output variables to monitor which are the angle θ_r and the intensity I_{max} of the reflected beam. We can track the evolution of both variables for different setups. In Fig. 6, we first study the effects of atom number N_a either keeping the number of disks N_d constant, therefore varying the atomic density N_a/N_d (left column) or keeping the density N_a/N_d constant (right column).

In both cases, the maximum reflected intensity increases by near a full order of magnitude from less than 10^{-6} to $\sim 9 \cdot 10^{-6}(u.a)$. Therefore, the density contributes only marginally to increase the maximum reflected intensity, and does not affect at all the reflection angle θ_r as it remains constant in both cases. Only the atom number N_a can lead to an increased maximum reflected intensity. Indeed, the more atoms there are, the more energy can be stored by exciting this larger population. Conversely, at constant density, very few atoms may be present to store the incident energy.

It should be noted that the slowdown in the increase of the maximum intensity is primarily due to the number of atoms, as well as to the optical depth, which enhances the absorption coefficient at resonance ($\Delta = 0$). Consequently, operating off-resonance becomes advantageous, as we shall discuss below.
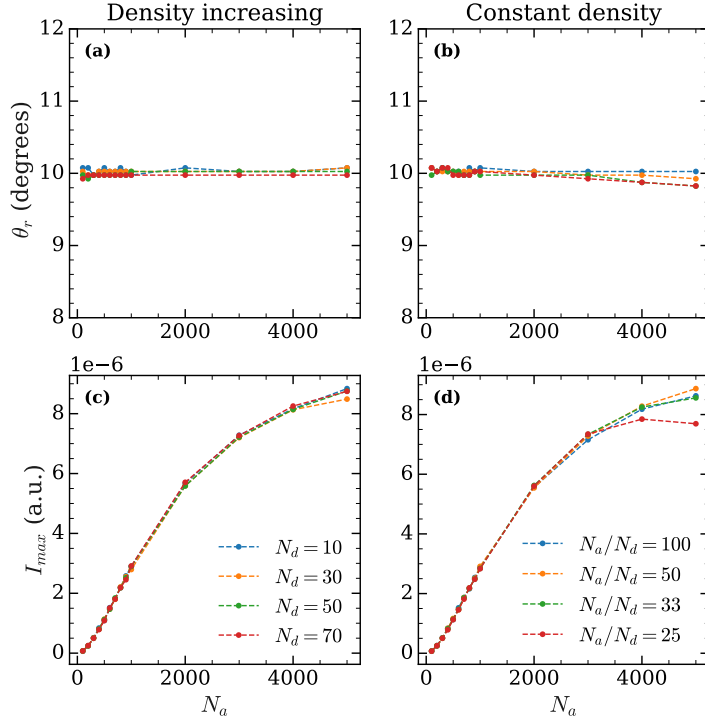
Fig. 6: In both cases, disks have thickness $a = 0.07$ and radius $R_d = 9\lambda$. Reflection angle θ_r and maximal reflected intensity $I_{\max}$ as function of atom number N_a, either keeping the number of disks constant ($N_d = 80$ on the left) or the density N_a/N_d constant (right column).

Fig. 7: Heatmap of reflectivity $R(\Delta, N_a)$ as a function of the detuning Δ and the number of atoms N_a. The lattice parameters are set to $N_d = 80$ disks of thickness $a = 0.07$ and radius $R_d = 9\lambda$, prepared in a Bragg scattering condition of $\theta = 5°$. The incident gaussian beam has a waist of $w_0 = 4\lambda$.

Since the beginning of this work, most parameters have been explored except for the detuning Δ and the laser properties. In Fig. 7, we present a 40×11 pixels heatmap of the reflection coefficient as a function of Δ and N_a, where the cells have been interpolated to produce the final result. For a fixed detuning, as shown in Fig. 6 and Fig. 7, increasing the number of atoms N_a enhances the reflected intensity. However, at resonance ($\Delta = 0$), the reflection coefficient begins to saturate, exhibiting a local minimum around $N_a = 4000$, which clearly corresponds to the slowdown in intensity growth observed in Fig. 6. Fig. 8 shows different horizontal cuts of Fig. 7 corresponding to different values of the atom number.

Fig. 8: Reflectivity slice for different N_a atoms count from previous heatmap in Fig. 7.

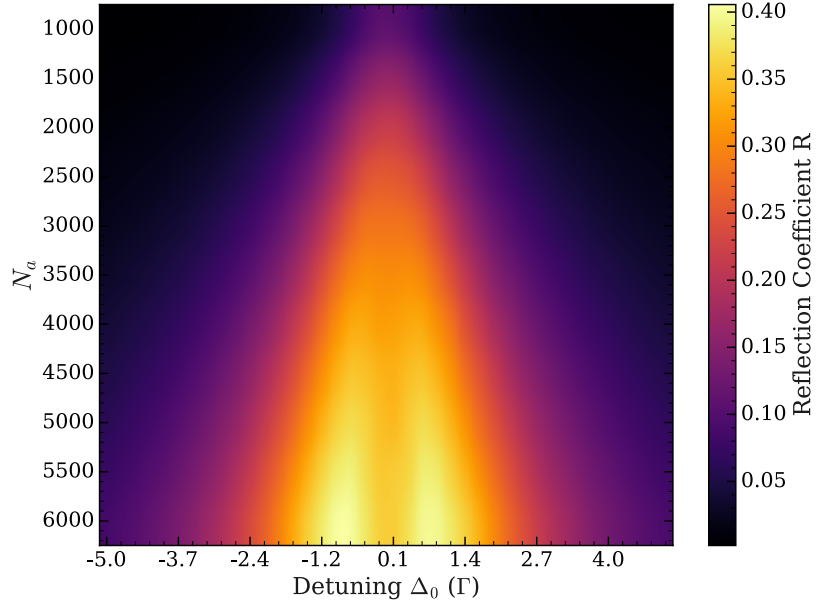Our next focus concerns the lattice periodicity d. As previously discussed in Fig. 5, the incidence angle θ_i plays a role similar to that of the lattice periodicity, apart from optical depth effects. However, we have only examined this effect with respect to the lattice periodicity, without considering the detuning. Therefore, we repeated the same analysis as in Fig. 7, this time varying the lattice periodicity, which was converted into a θ_{bragg} angle following (15).

Fig. 9: Reflectivity as a function of the detuning Δ and the lattice periodicity d converted in degress $\theta_{\text{bragg}} = \text{acos}(\lambda/2d)$. Each cell is the result of 100 iterations for $N_d = 80$ disks of thickness $a = 0.07$ and radius $R_d = 9\lambda$, prepared in a Bragg scattering condition of $\theta = 10°$. The incident Gaussian beam has a waist of $w_0 = 4\lambda$. The horizontal dotted line corresponds to $R(\Delta)$ with a lattice periodicity following Bragg condition of $10°$, which coincides with the $N_a = 5000$ plot in Fig. 8. The vertical dotted line corresponds to the plot in Fig. 5. The dot corresponds to the detuning used in later dynamics computation.

12

Lowering the lattice periodicity towards a smaller Bragg angle increases reflectivity for a redshifted laser, while increasing the lattice periodicity requires a blue-shifted laser to achieve optimal reflectivity, which agrees with experimental observation in [13]. Therefore, for larger atom numbers, it is often suboptimal to strictly follow Bragg's condition; instead, it is more effective to place the probe beam off-resonance and adjust the dipole trap wavelength λ_{dip} to obtain the optimal periodicity.

D. PBG with a resonant probe beam at 90° ($\Delta = 0$)

In this second part, we are interested to "bypass" the band gap by driving the lattice's atoms at a 90° angle and observing the system response. Keeping the same lattice parameters, in particular fulfilling Bragg condition at an angle $\theta_{\text{bragg}} = 10°$, we move the probe beam to an angle of $\theta_i = 90°$ to effectively drive the lattice to its stationnary regime.
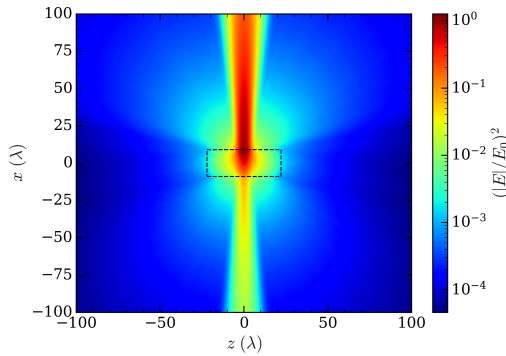

Fig. 10: Intensity of scattered light in the (xOz) plane with the same configuration as in Fig. 2 but with the probe beam at $\theta_i = 90°$.
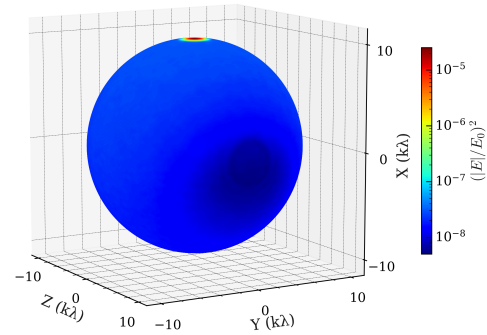

Fig. 11: Intensity of scattered light on the sphere at $R = 10^4\lambda$ for the same configuration as in Fig. 2 but with probe beam at $\theta = 90°$.

Similarly to the reflection case, there is a circular feature with an intensity bump at an angle of 10°, but this time it appears for all azimuthal angles (see Fig. 11 and Fig. 12). This bump actually corresponds to an intensity minimum, which appears as a slight step due to its finite width. For comparison, the same configuration was computed for a lattice periodicity of 25°, where a more pronounced local intensity minimum is observed.
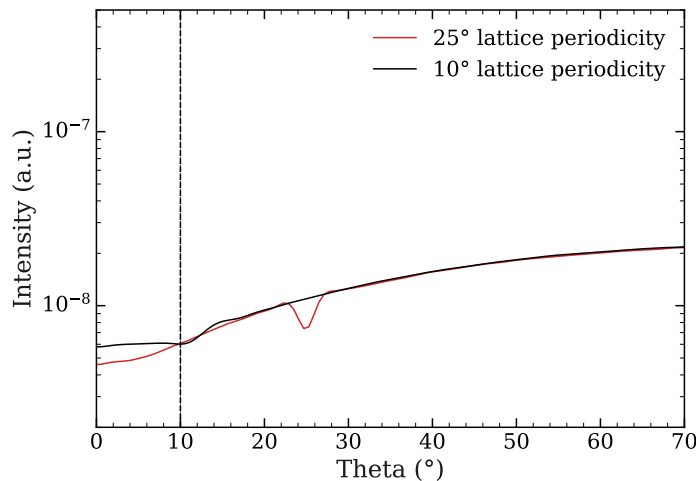

Fig. 12: Scattered intensity along θ direction with the same configuration as Fig. 2.

13

Finally, the slight step may be deepened to a true local minimum by increasing the number of disks (see Fig. 13). This selectivity can be readily explained through interference: while atoms collectively scatter light that does not interfere significantly, destructive interference occurs in the Bragg direction, resulting in the observed intensity minimum. However, it is still needed to fully understand how such collective behavior can emerge through dipole coupling.
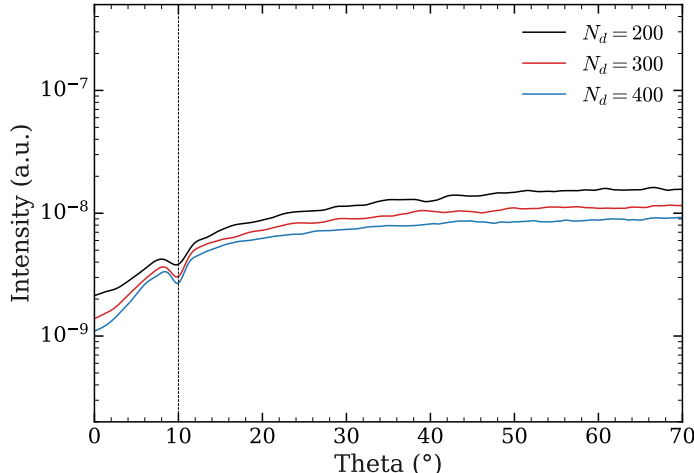

Fig. 13: Scattered intensity along θ direction with the same configuration as Fig. 2 but different disks count N_d.

IV. Dynamic scattering

Steady state of similar systems has been thoroughly studied theoretically [9,16] as well as experimentally in [10,11,13,14,17]. However, to the best of our knowledge, little research has been conducted on the decay dynamics of periodic medium of cold atom gases. A recent work [15] at the *Institute of Physics* in Nice experimentally observed a faster decay rate, called a super-radiant state, in the reflected direction, and is thus an interesting result that could be used to benchmark our numerical simulation.

A. Scattering dynamic with probe beam in reflection setup

The scattering dynamics are obtained by solving the coupled differential equations (10), where we set $E_L = 0$ and $\Delta = 0$ emulating an instantaneous probe beam cutoff. Nevertheless, the initial state, which is the steady state of (10), is still computed with nonzero values of Δ and E_L if chosen so. While the equation (10) could in principle be solved via eigenvalue methods, we opted instead for the 5th-order Runge–Kutta scheme proposed by Tsitouras [1] as it offers a sufficient precision and lower computational cost.

We plotted in Fig. 14 the normalized intensity over time for $N_a = 1000$ atoms distributed over $N_d = 80$ disks of radius $R_d = 9\lambda$ and thickness $a = 0.07\lambda$, with the initial state prepared using a resonant probe beam ($\Delta = 0$) at an incident angle of $\theta_i = 15°$. The chosen parameters correspond to a maximum reflectivity at 15° and to a lattice periodicity fulfilling the Bragg condition for this probe beam angle. For detection angles of 25°, 35°, and 45°, we observe similar decay rates, in contrast with the 15° direction that matches the Bragg condition. In this reflection direction, the decay rate is faster than in other directions, revealing a super-radiant state as reported in [15]. In most cases, the decay accelerates along the Bragg direction, while in other directions it slows down, as illustrated by the intensity respectively falling below or rising above both fits at short-term dynamics.
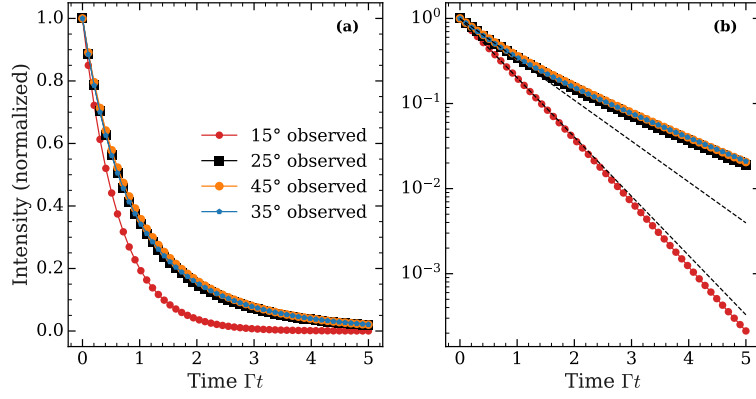
Fig. 14: Dynamic intensity for $N_a = 1000$ atoms distributed over $N_d = 80$ disks of thickness $a = 0.07\lambda$ and radius $R_d = 9\lambda$. The lattice satisifies the Bragg condition for $\theta = 15°$. The probe beam at an angle $\theta_i = 15°$ is resonant ($\Delta = 0.0$) which corresponds to a maximum of reflection. A linear fit in log-scale is shown for both the Bragg direction (15°) and other directions in (b).

Next, we plotted in Fig. 15 the halflife measured in each observation direction for different lattice periodicities d, converted into an equivalent angle according to (15). The halflife was chosen instead of an exponential fit, since short-term dynamics may not always follow a simple exponential decay. In this sense, the halflife provides a more model-independent characterization than a least-squares regression. It is worth noting that the decay rate can still be directly obtained from the halflife if needed.

Near the Bragg condition, we again observe a super-radiant state with the shortest lifetime among all lattice periodicities. Away from the Bragg condition, the halflife converges to the average decay rate of non-Bragg directions. However, at $\theta_{\mathrm{bragg}} = 8°$ and $13°$, two anomalous spikes in halflife appear, which cannot be explained by statistical fluctuations. As shown in Fig. 15, the intensity over time reveals a very slow initial decay followed by a rapid acceleration at later times, leading to a faster decay rate than in non-Bragg directions. This delayed "ignition" of the decay process results in a much larger halflife than expected. The long time decay rate remains slower than the one at $\theta_{\mathrm{bragg}} = 15°$.

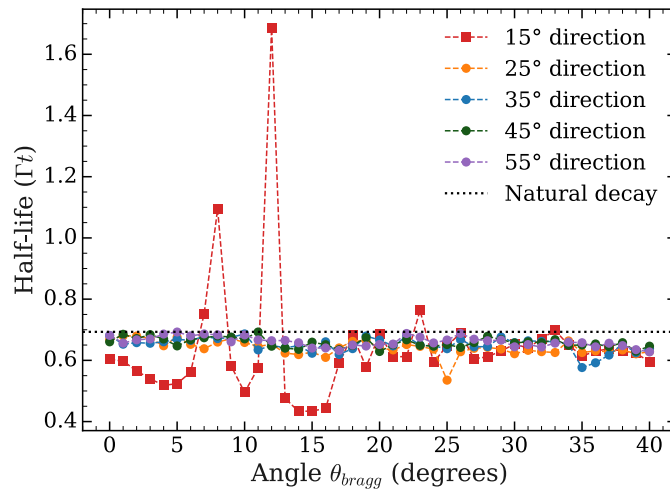Fig. 15: Half-life for the same parameters as in Fig. 14 but varying lattice periodicity d converted in degrees θ_{bragg}
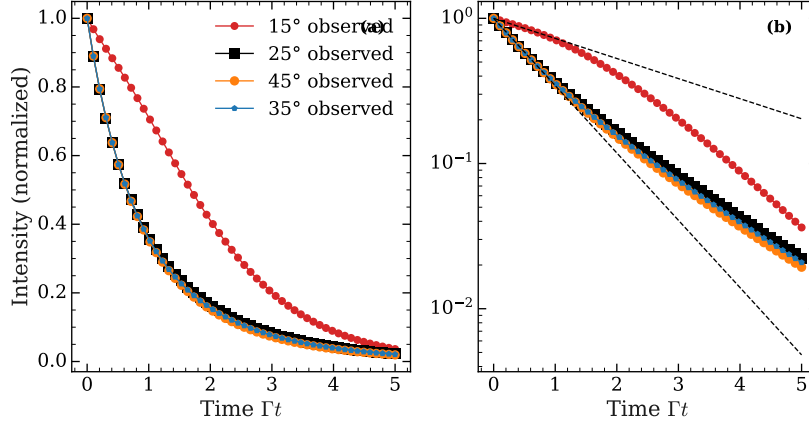
15

Fig. 16: Dynamic intensity for the same parameters as in Fig. 14 with lattice periodicity d set to $\theta_{\mathrm{bragg}} = 13°$ which corresponds to the second halflife spike in Fig. 15.

B. Scattering dynamic with probe beam in side setup

We performed the same analysis as in Fig. 15 using identical parameters, but with the probe beam oriented at $\theta_i = 90°$ to prepare the initial state. The corresponding results are shown in Fig. 17. For each detection direction, a clear correlation is observed between the observation angle θ and a pronounced reduction of approximately 10% in the halflife when approaching the Bragg condition, $\theta_{\mathrm{bragg}} \approx \theta$. This behavior indicates that our model consistently predicts the emergence of a super-radiant state in both reflection and side beam configurations, specifically near the Bragg angle.

In the side beam geometry, we further observe that the halflife tends to increase with larger observation angles, which may be attributed to a progressive departure from the Bragg condition and consequently weaker cooperative effects. These results remain theoretical at this stage and require experimental verification to assess their validity. In particular, the predicted reduction in halflife at the Bragg condition has not yet been demonstrated experimentally. However, it should be noted that the scalar model employed here cannot be used to quantitatively predict the modification of the halflife of the states.
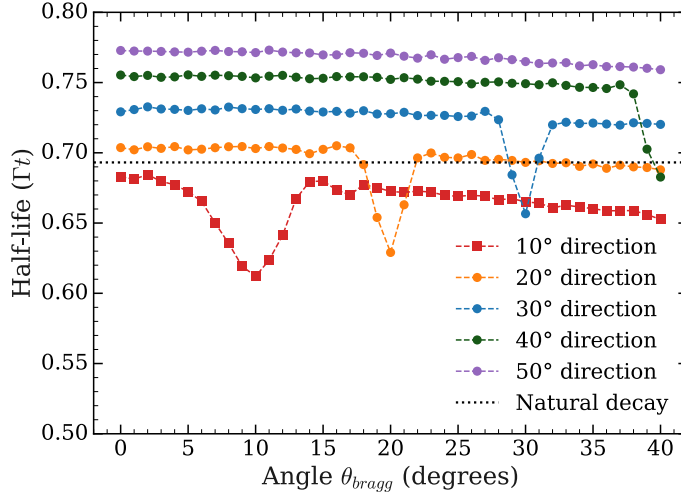

Fig. 17: Halflife over lattice periodicity for the same parameters as in Fig. 14 but probe beam is set at $\theta_i = 90°$ to prepare the initial state.

16

Finally, if the dependence of the halflife on the observation angle is confirmed, with shorter halflives observed at smaller θ, this property could potentially be exploited as a mechanism to control and selectively tune the effective lifetime of the stored information.

C. Difficulties encountered in dynamic computation

To conclude this study, we extended our simulations to a larger system consisting of $N_a = 5000$ atoms, distributed over $N_d = 200$ disks with thickness $a = 0.07\lambda$ and radius $R_d = 9\lambda$. The corresponding halflife dynamics were computed for both reflection and side beam setup, as shown in Fig. 18 and Fig. 19, respectively.

In the reflection configuration, we obtain results that are fully consistent with the trends observed in the previous sections: the halflife is significantly reduced, reaching nearly half of the non Bragg condition halflife, which is a clear signature of a super-radiant state. Interestingly, the minimum halflife does not occur exactly at the Bragg angle but appears slightly shifted, suggesting that the precise condition for constructive interference may depend on the system size and geometry.

In contrast, the side beam setup exhibits a more complex behavior. As shown in Fig. 19, we again observe a reduced halflife, but only for observation angles $\theta \gtrsim 20°$. At smaller angles, such as $\theta = 10°$, this reduction is absent, and similar deviations are also observed at other angular positions (not shown in Fig. 19 for the sake of readability). This angular asymmetry is not yet understood and suggests that additional mechanisms, beyond the current scalar model, may be influencing the cooperative decay.

At this stage, the origin of these features remains unclear and requires further investigation. Nevertheless, these results highlight both the robustness of the super-radiant state in reflection and the subtler, less intuitive behavior in side-detection, which may reveal new regimes of cooperative emission in extended atomic ensembles.
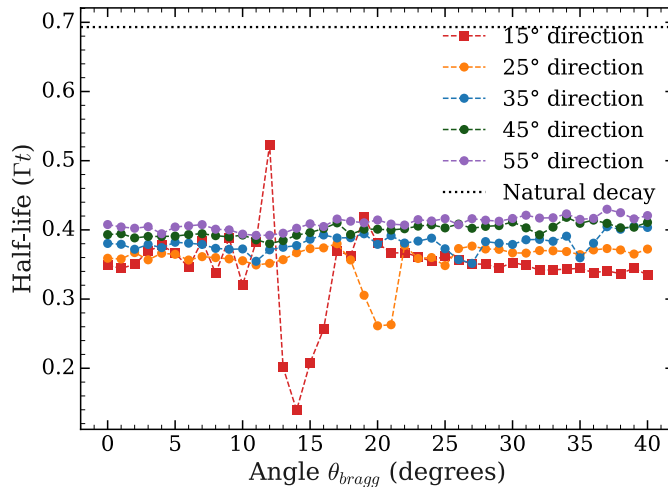

Fig. 18: Half-life with the lattice periodicity d varying for $N_a = 5000$ atoms distributed over $N_d = 200$ disks of thickness $a = 0.07\lambda$ and radius $R_d = 9\lambda$. Probe beam is non-resonant ($\Delta = -0.64\Gamma$ corresponding to a maximum of reflection) and at an angle $\theta_i = 15°$. The lattice periodicity d is converted in degrees θ_{bragg}.
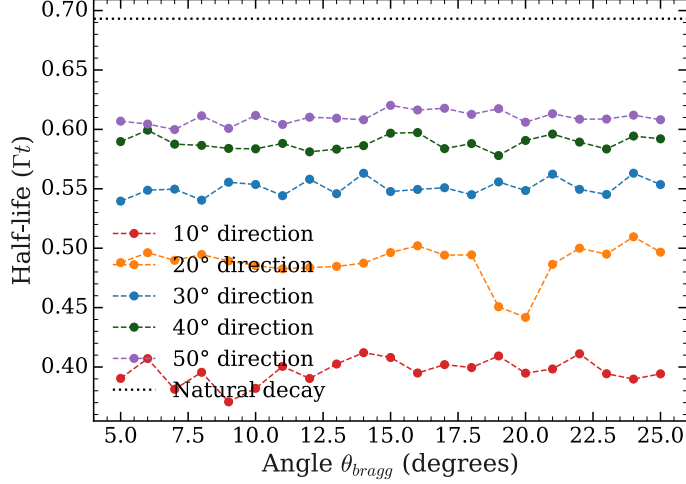
Fig. 19: Halflife along lattice periodicity with same parameters as in Fig. 18 but the probe beam is set in side configuration ($\theta_i = 90°$).

V. Conclusion

In this work, we investigated the collective scattering properties of cold atomic ensembles trapped in a one-dimensional optical lattice, with particular emphasis on the emergence of sub- and super-radiant states. Using a microscopic quantum model, we reproduced essential features already observed experimentally, such as Bragg reflection and the formation of a photonic band gap, while extending the analysis to dynamical regimes of collective decay.

In the stationary regime, our results demonstrated how reflectivity depends on the number of atoms, the lattice periodicity, and the detuning of the probe field. We confirmed the central role of optical depth and showed that off-resonant driving can optimize reflection efficiency, in agreement with experimental observations.

In the dynamical regime, our simulations highlighted the emergence of super-radiant states near the Bragg condition. Specifically, we observed a marked reduction of the halflife in both reflection and side-detection geometries, which is consistent with cooperative enhancement of emission. However, unexpected features were also identified, such as halflife anomalies at certain lattice periodicities and angular asymmetries in the side configuration, whose physical origin remains unclear.

It should be stressed that the scalar model employed here does not allow for a quantitative prediction of the halflife modification. Therefore, experimental verification remains essential to assess the validity and robustness of our conclusions.

References

[1] C. Tsitouras, Runge–Kutta pairs of order 5(4) satisfying only the first column simplifying assumption, Computers & Mathematics with Applications **62**, 770 (2011).

[2] C. Rackauckas and Q. Nie, Confederated modular differential equation APIs for accelerated algorithm development and benchmarking, Advances in Engineering Software **132**, 1 (2019).

[3] J. Bezanson, A. Edelman, S. Karpinski, and V. B. Shah, Julia: A Fresh Approach to Numerical Computing, SIAM Review **59**, 65 (2017).

[4] C. Rackauckas and Q. Nie, DifferentialEquations.jl – A Performant and Feature-Rich Ecosystem for Solving Differential Equations in Julia, Journal of Open Research Software **5**, (2017).

[5] U. Utkarsh et al., Automated Translation and Accelerated Solving of Differential Equations on Multiple GPU Platforms, Computer Methods in Applied Mechanics and Engineering **419**, 116591 (2024).

[6] R. H. Dicke, Coherence in Spontaneous Radiation Processes, Physical Review **93**, 99 (1954).

[7] A. Asenjo-Garcia, M. Moreno-Cardoner, A. Albrecht, H. J. Kimble, and D. E. Chang, Exponential Improvement in Photon Storage Fidelities Using Subradiance and "Selective Radiance" in Atomic Arrays, Physical Review X **7**, 31024 (2017).

[8] C.-R. Mann, F. Andreoli, V. Protsenko, Z. Lenarčič, and D. Chang, Selective Radiance in Super-Wavelength Atomic Arrays, (2024).

[9] R. Bachelard, N. Piovella, and P. Courteille, Cooperative scattering and radiation pressure force in dense atomic clouds, Physical Review a **84**, 13821 (2011).

[10] W. Guerin, M. O. Araújo, and R. Kaiser, Subradiance in a Large Cloud of Cold Atoms, Physical Review Letters **116**, 83601 (2016).

[11] M. Samoylova, N. Piovella, R. Bachelard, and P. W. Courteille, Microscopic theory of photonic band gaps in optical lattices, Optics Communications **312**, 94 (2014).

[12] A. Cipris, R. Bachelard, R. Kaiser, and W. Guerin, van der Waals dephasing for Dicke subradiance in cold atomic clouds, Physical Review a **103**, 33714 (2021).

[13] A. Schilke, C. Zimmermann, P. W. Courteille, and W. Guerin, Photonic Band Gaps in One-Dimensionally Ordered Cold Atomic Vapors, Physical Review Letters **106**, 223903 (2011).

[14] S. Slama, C. v. Cube, A. Ludewig, M. Kohler, C. Zimmermann, and P. W. Courteille, Dimensional Crossover in Bragg Scattering from an Optical Lattice, Physical Review a **72**, (2005).

[15] S. Asselie, J.-M. Nazon, R. Caldani, C. Roux-Spitz, and W. Guerin, Temporal dynamics in the Bragg reflection of light by cold atoms: flash effect and superradiant decay, (2025).

[16] T. Bienaimé, M. Petruzzo, D. Bigerni, N. Piovella, and R. Kaiser, Atom and photon measurement in cooperative scattering by cold atoms, Journal of Modern Optics **58**, 1942 (2011).

[17] W. Guerin, Super- and subradiance in dilute disordered cold atomic samples: observations and interpretations, **72**, 253 (2023).

[18] É. Gouzien, D. Ruiz, F.-M. Le Régent, J. Guillaud, and N. Sangouard, Performance Analysis of a Repetition Cat Code Architecture: Computing 256-bit Elliptic Curve Logarithm in 9 Hours with 126 133 Cat Qubits, Physical Review Letters **131**, 40602 (2023).

[19] N. Skribanowitz, I. P. Herman, J. C. MacGillivray, and M. S. Feld, Observation of Dicke Superradiance in Optically Pumped HF Gas, Physical Review Letters **30**, 309 (1973).

[20] H. Arai and T. Fujikawa, Keldysh's Green function approach to the radiation field screening in MARPE and XAFS, Physica Scripta **2005**, 1091 (2005).

[21] R. Friedberg, S. R. Hartmann, and J. T. Manassah, Frequency shifts in emission and absorption by resonant systems ot two-level atoms, Physics Reports **7**, 101 (1973).

[22] Z.-S. Yuan, Y.-A. Chen, B. Zhao, S. Chen, J. Schmiedmayer, and J.-W. Pan, Experimental demonstration of a BDCZ quantum repeater node, Nature **454**, 1098 (2008).

[23] C. Brechignac and P. Cahuzac, Observation of two visible Dicke-superradiant transitions in atomic europium (*), Journal De Physique Lettres **40**, 123 (1979).

[24] N. W. Carlson, D. J. Jackson, A. L. Schawlow, M. Gross, and S. Haroche, Superradiance triggering spectroscopy, Optics Communications **32**, 350 (1980).

[25] M. Gross, J. M. Raimond, and S. Haroche, Doppler Beats in Superradiance, Physical Review Letters **40**, 1711 (1978).

[26] A. Flusberg, T. Mossberg, and S. R. Hartmann, Observation of Dicke superradiance at 1.30 μm in atomic Tl vapor, Physics Letters a **58**, 373 (1976).

[27] A. Crubellier, S. Liberman, D. Mayou, P. Pillet, and M. G. Schweighofer, Oscillations in superradiance with long-duration pumping pulses, Optics Letters **7**, 16 (1982).

[28] M. Gross, C. Fabre, P. Pillet, and S. Haroche, Observation of Near-Infrared Dicke Superradiance on Cascading Transitions in Atomic Sodium, Physical Review Letters **36**, 1035 (1976).

[29] C. H. Bennett, G. Brassard, S. Breidbart, and S. Wiesner, *Quantum Cryptography, Or Unforgeable Subway Tokens*, in *Advances in Cryptology*, edited by D. Chaum, R. L. Rivest, and A. T. Sherman (Springer US, Boston, MA, 1983), pp. 267–275.

[30] É. Gouzien and N. Sangouard, Factoring 2048-bit RSA Integers in 177 Days with 13 436 Qubits and a Multimode Memory, Physical Review Letters **127**, 140503 (2021).

[31] A. Montanaro, Quantum algorithms: an overview, Npj Quantum Information **2**, 1 (2016).

[32] K. Hammerer, A. S. Sørensen, and E. S. Polzik, Quantum interface between light and atomic ensembles, Reviews of Modern Physics **82**, 1041 (2010).

[33] M. Gross and S. Haroche, Superradiance: An essay on the theory of collective spontaneous emission, Physics Reports **93**, 301 (1982).

[34] S. Slama, C. v. Cube, M. Kohler, C. Zimmermann, and P. W. Courteille, Multiple Reflections and Diffuse Scattering in Bragg Scattering at Optical Lattices, Physical Review a **73**, 23424 (2006).